

Kinetic Phase Evolution of Spinel Cobalt Oxide during Lithiation

Jing Li,^{†,‡} Kai He,^{†,⊥} Qingping Meng,[†] Xin Li,[§] Yizhou Zhu,^{||} Sooyeon Hwang,[†] Ke Sun,[†] Hong Gan,[†] Yimei Zhu,[†] Yifei Mo,^{||} Eric A. Stach,[†] and Dong Su^{*,†}

[†]Brookhaven National Laboratory, Upton, New York 11973, United States

[‡]Department of Materials Science and Engineering, Stony Brook University, Stony Brook, New York 11720, United States

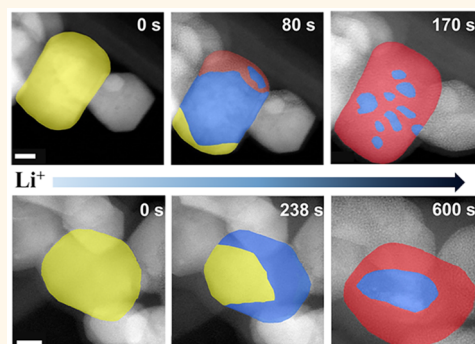
[§]John A. Paulson School of Engineering and Applied Sciences, Harvard University, Cambridge, Massachusetts 02138, United States

^{||}Department of Materials Science and Engineering, University of Maryland, College Park, Maryland 20742, United States

S Supporting Information

ABSTRACT: Spinel cobalt oxide has been proposed to undergo a multiple-step reaction during the electrochemical lithiation process. Understanding the kinetics of the lithiation process in this compound is crucial to optimize its performance and cyclability. In this work, we have utilized a low-angle annular dark-field scanning transmission electron microscopy method to visualize the dynamic reaction process in real time and study the reaction kinetics at different rates. We show that the particles undergo a two-step reaction at the single-particle level, which includes an initial intercalation reaction followed by a conversion reaction. At low rates, the conversion reaction starts after the intercalation reaction has fully finished, consistent with the prediction of density functional theoretical calculations. At high rates, the intercalation reaction is overwhelmed by the subsequently nucleated conversion reaction, and the reaction speeds of both the intercalation and conversion reactions are increased. Phase-field simulations show the crucial role of surface diffusion rates of lithium ions in controlling this process. This work provides microscopic insights into the reaction dynamics in non-equilibrium conditions and highlights the effect of lithium diffusion rates on the overall reaction homogeneity as well as the performance.

KEYWORDS: Co_3O_4 nanoparticles, lithium-ion battery, in situ TEM



Rechargeable lithium-ion batteries have gained tremendous attention in applications such as portable devices because of their high energy density and high voltage when compared to other battery technologies.^{1,2} To ensure a better user experience with portable electronics, improvement of battery performance is critical, particularly to reduce the size and increase the charging rate without sacrificing energy density. These requirements are reflected from a materials perspective in the demand for the development of advanced electrode materials with higher volumetric energy density and better rate capability. Specifically, with respect to rate capability, there have been significant efforts to improve material properties through both synthetic and engineering approaches and to uncover the mechanisms of reaction through the use of multiple characterization and calculation methods. These studies have made clear the important role of kinetics in controlling electrochemical reactions within electrode materials.^{3–6} Transition metal oxides have attracted extensive attention since Poizot *et al.* demonstrated their feasibility as conversion electrode materials for lithium-ion batteries.^{7,8} Recent studies have shown the correlation of rate capability

with microscopic reaction pathways in nickel oxides, where only a simple conversion reaction occurs.⁹ However, for other complex oxides with extra interstitial openings in their crystal lattices (*e.g.*, spinel), where both lithium insertion and conversion can happen, the competitive reaction kinetics of these two reactions may affect the rate-dependent behaviors.

Spinel cobalt oxide (Co_3O_4) has a theoretical capacity of 890 mAh/g, making it an important candidate for anodes.^{10–13} Its structure is in the form of AB_2O_4 , where A and B sites are both cobalt, but A is at the tetrahedral 8a (Wyckoff) site and B is at the octahedral 16d site. Thackeray *et al.* have investigated the reaction mechanism of the chemical lithiation of Co_3O_4 .¹⁰ In the initial stage of lithiation, Li ions are inserted into spinel Co_3O_4 , displaced, and push the Co^{2+} at the 8a site into the adjacent octahedral 16c site to form a rock-salt structure ($\text{Li}_x(\text{Co})_{16c}[\text{Co}_2]_{16d}\text{O}_4$ ($x < 1$)). This is an intercalation

Received: July 25, 2016

Accepted: September 15, 2016

Published: September 15, 2016

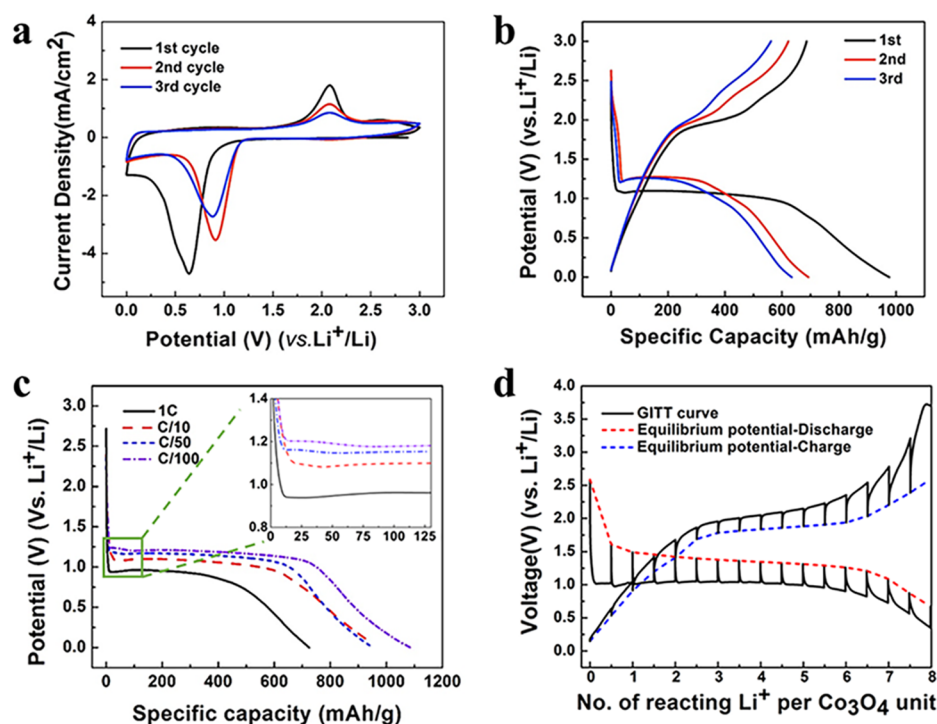
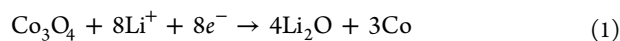


Figure 1. Electrochemical performances of Co₃O₄. (a) First three cyclic voltammogram curves of the Co₃O₄ electrode in the range of 0.01–3.00 V. (b) Discharge and charge profiles of the Co₃O₄ electrode at a rate of 0.1C in the range of 0.01–3.00 V. (c) Discharge profiles of the Co₃O₄ electrode in the range of 0.01–3.00 V at rates of 1C (black line), 0.1C (red dashed line), 0.02C (blue dashed line), and 0.01C (violet dashed line). The inset image presents magnified curves in the range of 0 to 125 mAh/g. (d) Charge and discharge galvanostatic intermittent titration technique curves of the Co₃O₄ electrode.

process, and the octahedral framework of the 16d site is maintained with only a very small volume change. It was suggested that Li_xCo₃O₄ is not stable, and several possible reactions would happen in the presence of the electrolyte;¹⁰ with further lithiation, incoming Li ions will occupy the 8a site and then push Co ions at the 16d site out of the framework, thereby triggering an extrusion reaction. In the final stage of lithiation, the compound will be decomposed into a nano-composite composed of Li₂O and metallic Co (hcp structure), which is a conversion reaction.^{10–13} In total, there are up to eight Li ions that can be stored per formula unit. The overall reaction equation is



This intercalation–conversion reaction pathway provides a great platform to study kinetic effects in multiple reaction conditions. Under a certain potential, the reaction kinetics can be described by the Butler–Volmer equation, where current density depends on the surface overpotential and the nature of the interface between the electrolyte and electrode.¹⁴ In addition—due to local inhomogeneity present in the electrode composites—the action of side reactions and differing diffusion pathways may also strongly affect the reaction process.^{3–9} Because of these complicated issues, and despite intensive efforts to improve battery performance using nanosized Co₃O₄ with different morphologies (nanowire, mesoporous, graphene composite, nanocage, etc.),^{15–22} the dynamical process that occurs during the evolution of these phases is still not fully understood because the electrochemical reactions in real batteries are highly heterogeneous and can be more complicated than the scenario described in the thermodynamic equilibrium state.³

Although many studies have been able to provide structural information about the electrochemical lithiation,²³ there are still challenges to overcome. For example, due to the relaxation of the electrochemical system after discharge/charge, *ex situ* characterization approaches are not capable of investigating these dynamical processes.²⁴ Commonly used *in situ* X-ray methods can probe dynamical phenomena, but such techniques may not be able to properly characterize nanosized electrode materials, as their dimensions reach the scale of 100 nm.^{24–26} Alternatively, *in situ* transmission electron microscopy (TEM) is a specialized technique that is able to study structural changes down to the nano- and atomic scale and has been successfully applied to study the dynamics of lithiation processes such as alloying and conversion reactions that involve significant volume changes.^{9,23,27–38} However, for intercalation reactions, where the lattice parameters only change a few percent, the dynamics of phase evolution are still difficult to probe using traditional *in situ* TEM methods. Here, we use a strain-sensitive, low-angle annular dark-field (LAADF) scanning TEM (STEM) technique to directly visualize the phase evolution processes that occur, even when volume changes are small.³⁹ We are able to observe the intercalation reaction process of Co₃O₄ in real time during the initial discharge and the subsequent conversion reaction at different kinetic conditions. It is observed that the rock-salt intermediate phase is always present, independent of reaction rates. We also find that the nature of the reaction may be strongly affected by the lithium diffusion onto the particles. These *in situ* STEM results, which are shown to be consistent with both density functional theory (DFT) calculations and phase-field simulations, provide valuable insight into electrochemical performance at different rates.

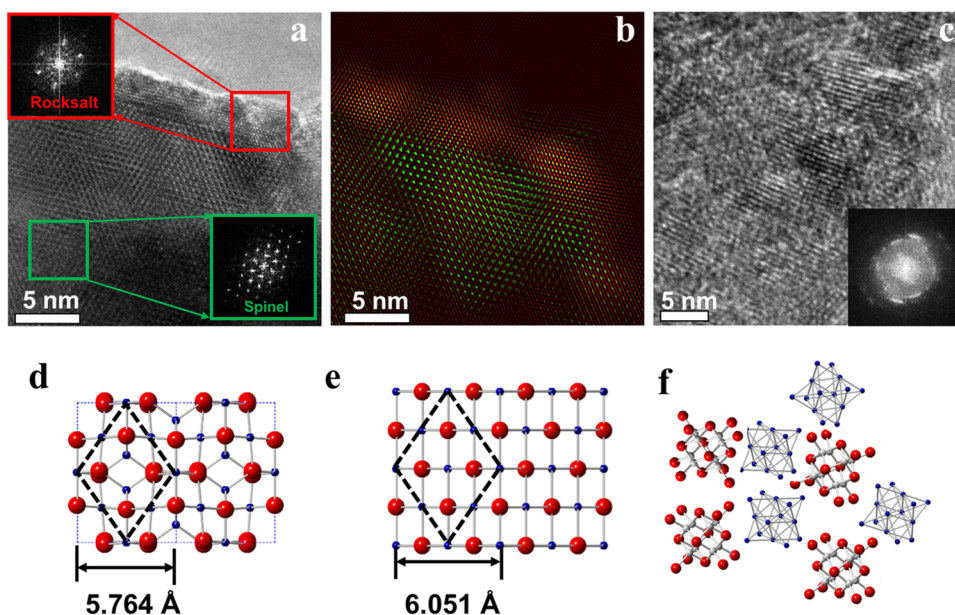


Figure 2. (a) HRTEM image of a Co_3O_4 nanoparticle indicating the coexistence of both spinel and rock-salt structure. Insets show the FFT of the spinel structure (green) and rock-salt structure (red) along the $[011]$ zone axis. (b) Filtered images of (a) show the corresponding phase distribution using two sets of spinel and rock-salt FFTs. (c) HRTEM images of the composite electrode after the conversion reaction. (d–f) Atomic structures of pristine Co_3O_4 with spinel structure, rock-salt ($\text{Li}_x\text{Co}_3\text{O}_4$), and composite of Li_2O plus metallic Co, respectively.

RESULTS AND DISCUSSION

First, we investigate the electrochemical behavior of as-prepared Co_3O_4 nanoparticles using cyclic voltammetry (CV), galvanostatic discharge–charge experiments, as well as the galvanostatic intermittent titration technique (GITT). Figure 1a illustrates the first three cycles of CV curves of the Co_3O_4 electrode cycled between 0 and 3 V at a rate of $C/10$ (1 lithium insertion per formula in 1.25 h). During the first cycle, a profound reduction peak was observed at 0.66 V that has been proposed to be caused by the initial reduction of Co_3O_4 to metallic Co.^{13–16} Meanwhile, the peak at 2.32 V is observed in the oxidation process and has been assigned as the oxidation of Co to CoO , with the decomposition of Li_2O according to ref 18 (also as shown in Supplementary Figure S1). In subsequent cycles, the reduction peaks shift to around 0.9 V, corresponding to the reduction of CoO to metallic Co.^{12,19} Figure 1b shows the discharge and charge profiles for cycles 1–3 at a rate of $C/10$. A plateau is observed at 1.14 V for the first cycle. For the second and third discharge curves, the potential of the plateau increases to 1.25 V due to less polarization. The results of CV and charge–discharge profiles are consistent with the prior reports.^{13,15–22}

We also measured the discharge profiles at different C rates, as shown in Figure 1c. A higher capacity can be achieved at a lower rate of $C/100$; for example, the initial capacity at $C/100$ is 1080 mAh/g, whereas it is 725 mAh/g at $1C$. This inverse relationship between capacity and charge rate (rate capability) is commonly observed in most battery systems. For the first discharge (lithiation) cycle at rates of $C/1$ and $C/10$, we have not observed multiple plateaus that would correspond to transitions from Co_3O_4 to LiCo_3O_4 or from LiCo_3O_4 to Co, whereas we found these two plateaus at rates of $C/50$ and $C/100$ as shown enlarged in the figure inset. In the curve of $C/100$, the first plateau is at about 1.23 V and ends at about 100 mAh/g in discharge capacity, equal to nominal 0.9 Li insertion; then the second plateau drops to a voltage of 1.20 V. We

suspect that those two plateaus may correspond to intercalation and conversion reactions, respectively. However, because the potential values of the plateau are changing due to the polarization at different C rates, it is not reliable to directly attribute these two plateaus to certain reactions. In addition, we observed that the capacity at $C/100$ is even higher than the theoretical capacity (890 mAh/g), which should be due to the side reactions between the active material and electrolyte.⁹ These side reactions consuming the extra lithium result in the formation of a surface layer and are supposed to be more severe under low rate charging due to a longer reaction time.⁹ To evaluate the state close to the equilibrium state, we have performed a GITT analysis at $C/10$, where at certain states of discharge we measure the open-circuit voltage (OCV) after a 24 h relaxation. We indeed observed a 0.3–0.5 V gap between the relaxed curve (red and blue dashed lines) and the plateau of $C/10$. In addition, the relaxed curve has a bump that ends at around $x = 1$. This is consistent with the discharge curve at $C/100$, which confirmed the appearance of the first plateau at a low discharge rate.

Thereafter, we performed high-resolution phase contrast TEM (HRTEM) imaging on the Co_3O_4 sample along the $\langle 110 \rangle$ zone axis after 25% of a full discharge. At this early stage of discharge, we observed the formation of a rock-salt phase at the surface of single nanoparticles, as shown in Figure 2a. The insets of Figure 2a show the selected area fast Fourier transform (FFT) from the bulk (green) and surface (red): these correspond to the spinel and rock-salt phases, respectively. The filtered image in Figure 2b further shows the distribution of these two phases. As indicated in the models of their crystal structures shown in Figure 2d,e, the spacing of one unit cell along the $\langle 110 \rangle$ projection in the spinel phase (5.764 Å) is close to that in the rock-salt phase (6.051 Å). Therefore, the interfacial strain between these two phases is supposed to be minimized, which helps to reduce the internal strain. As shown in Figure 2c, which was obtained from a fully lithiated sample, a composite structure is formed which contains reduced Co

nanoparticles and Li_2O , similar to other metal oxide conversion compounds. This is confirmed by the selected area electron diffraction (SAED) and electron energy loss spectroscopy (EELS) in Figure S1.

To investigate the dynamics of the phase evolution, we have employed an *in situ* dry cell technique, as utilized in previous reports.^{9,32,33,40,41} Since the electrochemical environment in this approach can be different from that found in conventional coin cells, which use an organic electrolyte, we first performed *in situ* electron diffraction from the sample throughout the entire lithiation process of Co_3O_4 to confirm the reaction, as shown in Figure 3 and Movie 1. The profiles of a series of

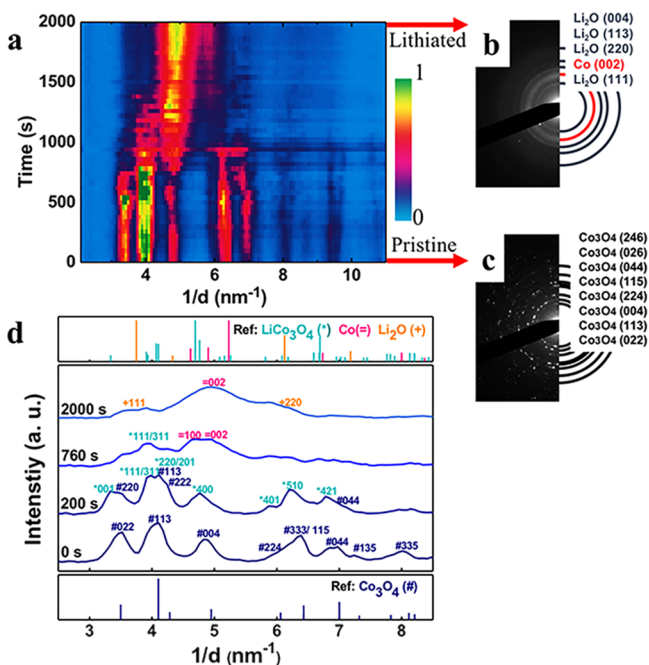


Figure 3. *In situ* selected area electron diffraction results, showing the phase evolution during lithiation. (a) Electron diffraction intensity profile as a function of reaction time during *in situ* lithiation of Co_3O_4 nanoparticles. (b,c) SAED patterns corresponding to the intensity profile obtained at the lithiated (2000 s) and pristine (0 s) state. (d) Integrated intensity profiles at 0, 200, 760, and 2000 s are indexed with respect to references Co_3O_4 , LiCo_3O_4 , Co, and Li_2O phases.

SAED are plotted as a function of reaction time, shown by a false color map in Figure 3a. From this, we extracted the SAED patterns of the pristine and fully lithiated sample, respectively, in Figure 3b,c. These patterns confirm that the phase transforms from spinel Co_3O_4 to a composite of metallic Co (hexagonal close-packed (hcp) phase) and Li_2O (cubic phase) after the lithiation process. The diffraction profiles at 0, 200, 760, and 2000 s are plotted and indexed in Figure 3c. We note that because of the overlapping of the peaks (e.g., Co_3O_4 (113) vs LiCo_3O_4 (111) and others), it is difficult to identify the evolution of the intermediate phase ($\text{Li}_x\text{Co}_3\text{O}_4$) that was confirmed by HRTEM images in Figure 2. Another *in situ* SAED result is shown in Figure S2 and Movie 2. We can trace the phase change of spinel, but it is difficult to unambiguously attribute any specific peak to the $\text{Li}_x\text{Co}_3\text{O}_4$ phase. This is because selected area diffraction samples are $\sim 1 \mu\text{m}$, and thus several phases can be present at the same time due to the highly inhomogeneous nature of the reaction.

Thereafter, we utilized *in situ* LAADF-STEM imaging to investigate the lithiation process in real space, as shown in Figures 4 and 5 as well as Movie 3 and Movie 4 (accelerated by 38 times and 12 times, respectively). In the case of LAADF-STEM imaging, the contrast can be attributed from both atomic (Z) contrast and diffraction contrast, while the contrast of a bright-field (BF)-STEM image is from the mixture of diffraction contrast and phase contrast. Therefore, a BF-STEM imaging technique containing diffraction contrast can also work in this case.³³ On the other hand, the Z-contrast HAADF-STEM imaging technique is proven to not be sensitive to observe the intercalation reaction. The key experimental point in the utilization of this imaging technique is to use a low collection angle (the inner angle ~ 15 mrad in our case) to detect the contraction in the lattice induced by the strain and also to avoid bending contours. Figure 4a presents a time sequence of LAADF-STEM images at a relatively low lithiation rate. Here, the overall lithiation rate is controlled by the voltage applied at the tip of the nanofactory holder. The local diffusion rate of lithium can be affected by the overall rate, but we note that no direct correlation can be made between the overall rate and local lithium concentration. In these experiments, we are able to observe—from differences in both their contrast and morphology—the evolution of the spinel Co_3O_4 into the intermediate phase $\text{Li}_x\text{Co}_3\text{O}_4$ and finally into a composite composed of Li_2O and Co. These phases are false colored with yellow, blue, and red, respectively, while the raw images are shown in Figure S3. The lithiation process is driven by the diffusion of lithium ions from right to left. In the initial stage, because the lattice mismatch between $\text{Li}_x\text{Co}_3\text{O}_4$ and Co_3O_4 phases is only 4.74%, there is no obvious volume change. However, a contrast change was observed, and this contrast change is attributed to the nucleation and growth of the $\text{Li}_x\text{Co}_3\text{O}_4$ phase. In this experiment, it takes about 334 s for the spinel phase to be fully converted to the rock-salt phase. Further lithiation triggered the conversion reaction and led to a large volume expansion. Up to the end of this movie at 600 s, the conversion reaction is still not finished. The projected areas as a function of reaction time are plotted in Figure 4b.

We also investigated the lithiation process at a higher rate, which leads to a different reaction nature than was observed in the experiment presented in Figure 4. A time sequence of LAADF-STEM images from this experiment is present in Figure 5a, with the phases of spinel, rock-salt, and composite being false-colored with yellow, blue, and red, respectively. The corresponding raw images are presented as Figure S4. The faster lithium diffusion increased the reaction kinetics: in this condition, the conversion reaction started later than the intercalation process but propagated in parallel through “finger-like” penetration pathways. These pathways were observed to be highly affected by the local strain and acted to increase the reaction speed.⁸ We measured the projected area changes as a function of time, though these measurements were necessarily approximate because of the overlap of projected images in some portions (Figure 5b). From the results of Figure 4b and Figure 5b, we can quantify and compare the rate at which the spinel phase shrinks in size, as well as the rate of growth of the composite, as shown in Figure 5c. In our experiments, we have not observed any cases where the intercalation reaction was simply bypassed, as had been proposed to occur at high rates.¹³ Instead, the two-step reaction is maintained, with these two phases coexisting within one single particle. If it is assumed that the Co_3O_4 nanoparticles

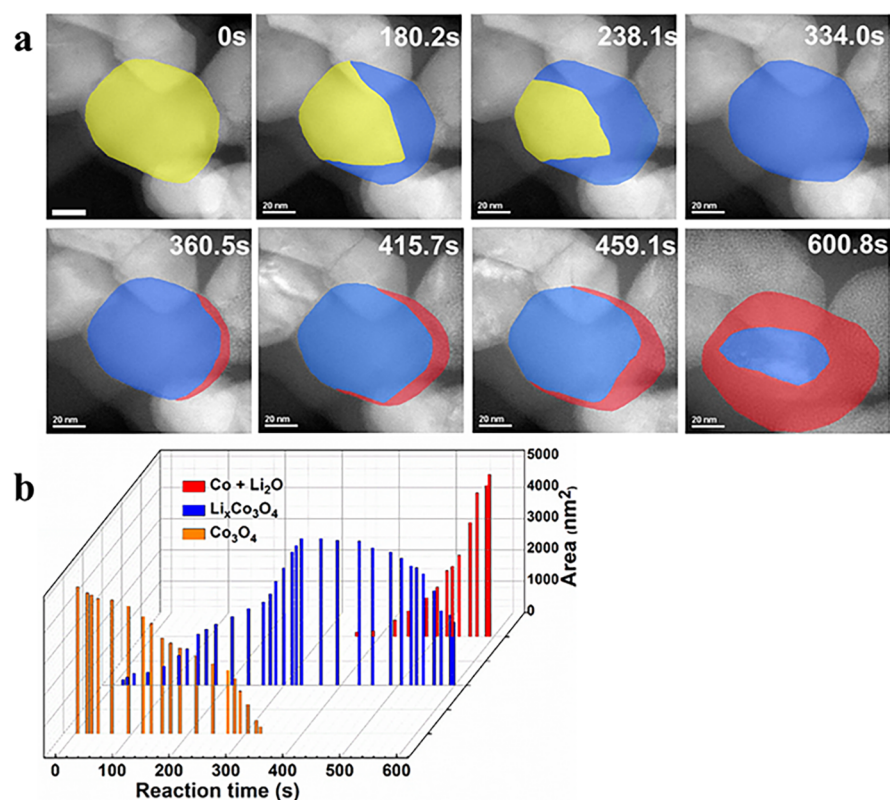


Figure 4. *In situ* morphological evolution of Co_3O_4 during lithiation at a low rate. (a) LAADF-STEM image series shows phase evolution during lithiation in real time. To clarify the distribution and route of different phases, three overlaid false colors are used: yellow (pristine Co_3O_4), blue (intermediate phase $\text{Li}_x\text{Co}_3\text{O}_4$), and red (composition of Co and Li_2O after conversion). Scale bar is 20 nm. Raw data are presented as [Supplemental Figure S3](#) (b) Projected areas of three phases as a function of reaction time (0–600.8 s).

have an identical surface nature, the average reaction speed observed by *in situ* TEM is expected to be controlled primarily by the concentration of Li ions at the surface of the Co_3O_4 nanoparticles (*i.e.*, the lithiation rate) in our experiments. For the higher reaction speed, we suspect there is a higher Li concentration than is present at the lower speed: we will present simulations using the phase-field theory later in the text which support these conclusions.

The reaction pathway in equilibrium can be calculated using DFT.^{42–45} [Figure 6a](#) presents calculated voltage profiles for the lithiation of Co_3O_4 to form the $\text{Li}_2\text{O} + \text{Co}$ composite. The calculated profile in the equilibrium state has multiple voltage plateaus (green dashed line) with multiple intermediate phases, such as LiCoO_2 , Li_2CoO_2 , and Li_5CoO_4 . Given both that LiCo_3O_4 is an intermediate phase experimentally observed from HRTEM imaging and the nature of two-step reaction, we also considered an alternative route (red solid line), which includes the intercalation plateau ($\text{Li} + \text{Co}_3\text{O}_4 \rightarrow \text{LiCo}_3\text{O}_4$) and the conversion plateau ($\text{LiCo}_3\text{O}_4 \rightarrow \text{Li}_2\text{O} + \text{Co}$). The ground state LiCo_3O_4 structure used in the DFT computation is constructed based on the structure observed in the HRTEM images in [Figure 2](#), consistent with the proposed Li-ion intercalation process. However, experimentally, the two-plateau profile (red) is only observed at very low discharge rate, as shown in [Figure 1c](#). As shown by the *in situ* results in [Figure 5](#), high current/lithium supply may kinetically modify the reaction pathways. Here, we simulated the process by which Li ions insert into the structure using a non-equilibrium phase-field simulation, developed by Bazant and his collaborators.^{46,47} To describe the diffusion behavior of Li ions and the phase evolution

([Figure 6b](#)), we have combined the Butler–Volmer equation ([eq 2](#)) for the surface of electrolyte and particles:

$$\frac{\partial c}{\partial t} = I_0 \left[\exp\left(-\frac{\alpha n e \eta}{k_B T}\right) - \exp\left(\frac{(1-\alpha) n e \eta}{k_B T}\right) \right] \quad (2)$$

and the Cahn–Hilliard model ([eq 3](#)) for the interior of particles:⁴⁶

$$\frac{\partial c}{\partial t} = \nabla M c \nabla (\Delta \mu) \quad (3)$$

to simulate the revolution of phase. The resulting chemical potential is thus⁴⁸

$$\Delta \mu = \frac{\partial f}{\partial c} - \kappa \nabla^2 c \quad (4)$$

This is derived from the homogeneous concentration-dependent free energy (f) and the Cahn–Hilliard gradient energy coefficient (κ). The other parameters in [eqs 2](#) and [3](#), as well as additional numerical details, can be found in the [Supporting Information](#). In comparison with our previous calculation, we have further included a contribution from strain energy due to the volume extension during the conversion reaction. Additionally, η is the activation overpotential; ne is the net charge transferred from the solution to the electrode; k_B is the Boltzmann constant, and T is temperature. In order to study how current affects the nature of the reaction, we have used two different current values of 0.001 and 0.01 in the simulations. [Figure 6c,d](#) presents time-sequenced Li composition profiles inside the crystal at different currents, as determined from

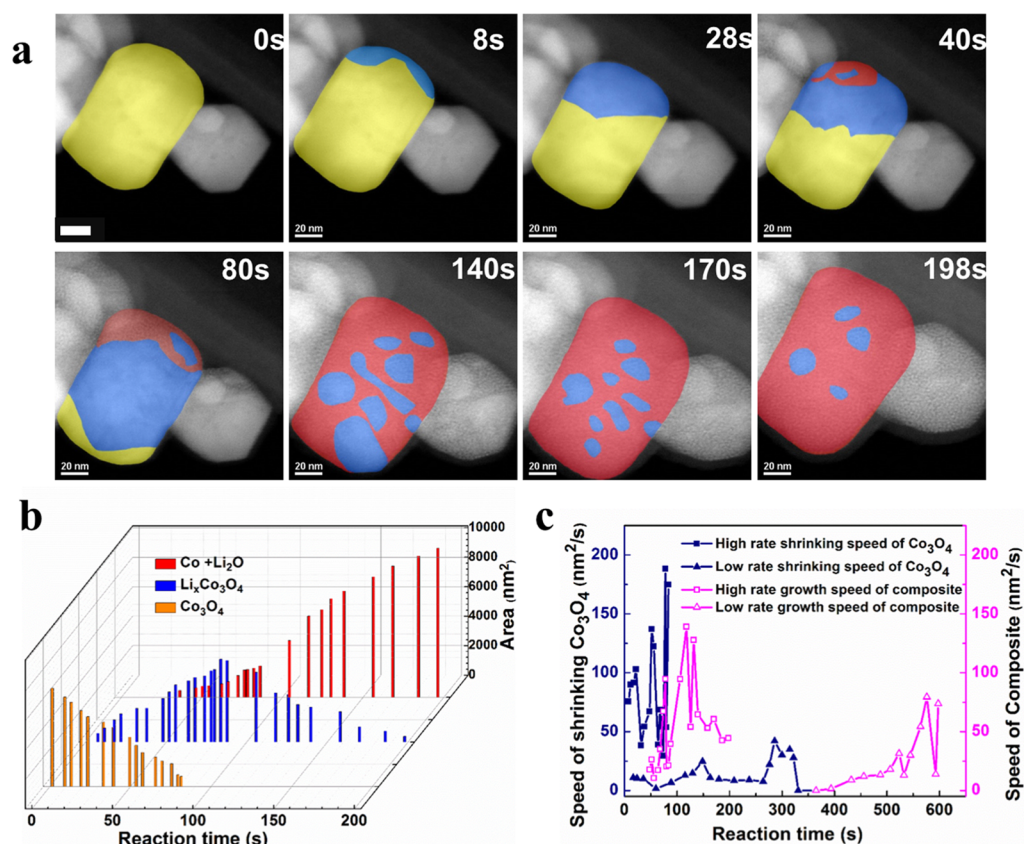


Figure 5. *In situ* morphological evolution of Co_3O_4 during lithiation at a high rate. (a) LAADF-STEM image series show phase evolution during lithiation as a function of reaction time (0–198 s). To clarify distribution and the route of different phases, three overlaid false colors are used: yellow (pristine Co_3O_4), blue (intermediate phase $\text{Li}_x\text{Co}_3\text{O}_4$), and red (composition of Co and Li_2O after conversion). Scale bar is 20 nm. Raw data are presented as Supplemental Figure S4. (b) Projected areas of three phases as a function of reaction time. (c) Comparison of shrinking/propagation speed between the results shown in Figure 4a and panel a in this figure.

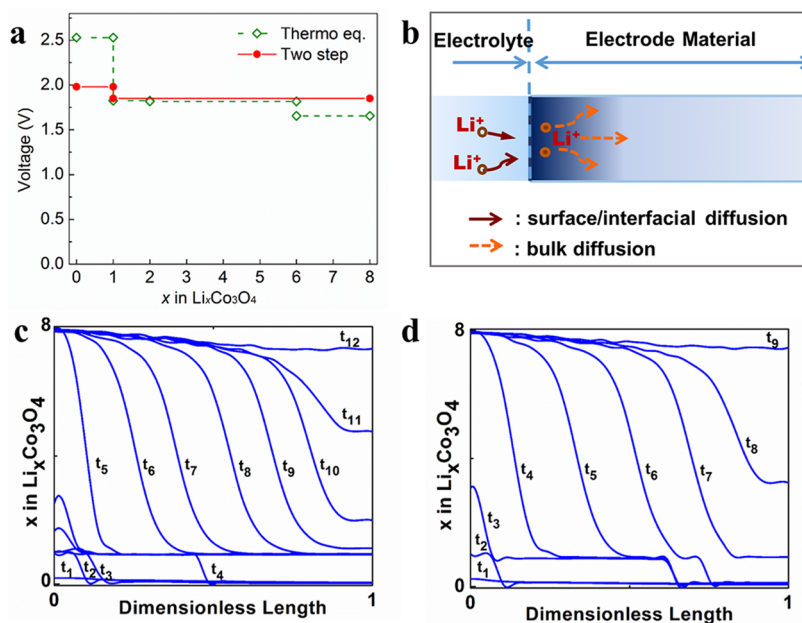


Figure 6. Theoretical calculations: (a) Discharge voltage profiles as a function of Li composition in $\text{Li}_x\text{Co}_3\text{O}_4$ ($x = 0$ – 8) calculated from first-principles calculation. The thermodynamic equilibrium reaction route is shown as green dashed lines, and the two-step reaction route is shown as red solid lines. (b) Schematic diagram illustrates the diffusion behavior of Li^+ ions on the surface between the electrolyte and the electrode, as well as in the interior of the electrode. (c,d) Li composition profiles along a one-dimensional length as a function of reaction time, as simulated by the phase-field theory (also see Movies 5 and 6).

Movie 5 and **Movie 6**. The nature of the reaction shown in **Figures 4** and **5** is reproduced very well by these simulations. First, the rock-salt LiCo_3O_4 phase (at $x = 1$) forms with increasing Li-ion concentration at the surface. The conversion reaction occurs subsequently, caused by the increased concentration of Li ions at the surface. At low rates, the conversion reaction nucleates when the intercalation reaction has nearly completed, while at high rate, the conversion reaction may nucleate early and can be overlapped with the intercalation reaction. Afterward, the conversion phase expands until the sample is fully lithiated. Both the *in situ* STEM experiments and the phase-field simulations capture the nature of the two-step reaction from Co_3O_4 to a composite of Co and Li_2O . In general, we have found that the dynamic lithiation process follows the multistep procedure suggested by Thackeray *et al.*¹⁰ However, after the formation of the rock-salt phase, we do not observe the extrusion of lithium or cobalt, which is supposed to be an intact particle with only the formation of metallic fine nanoparticles on the surface, whereas we observe the particle shrinking due to the conversion process. The absence of the extrusion process may be because they happen either at higher temperature (50 °C) or only in the presence of oxidizing agents. It was proposed that the fast discharge may trigger a direct conversion reaction of $\text{Co}_3\text{O}_4 + \text{Li} \rightarrow \text{Co} + \text{Li}_2\text{O}$;¹³ however, in our *in situ* experiments, we did not observe this direct conversion reaction. Instead, we found an accelerated conversion reaction which happened in parallel with the intercalation reaction.

CONCLUSIONS

We have investigated the lithiation of spinel Co_3O_4 using electrochemical analysis as well as *in situ* and *ex situ* TEM. Besides confirming the formation of $\text{Li}_x\text{Co}_3\text{O}_4$ through the use of high-resolution TEM, we have directly visualized the dynamic reaction process in real time using ADF-STEM imaging. These *in situ* experiments showed that a two-step reaction occurs, wherein an initial intercalation reaction is followed by a conversion reaction. Furthermore, at high current rates, we found that a fast intercalation reaction is initiated, and that this fast reaction may lead to an intermediate state, wherein the intercalation reaction is subsequently overwhelmed by the faster propagating conversion reaction. The reaction speed of both intercalation and conversion are enhanced at high rates by fast diffusion rates of lithium ions at the surface of the material. In addition, we found that the reaction can proceed by a “finger-like” penetration mode when the process is driven at high rates, and that this may further increase the speed of the conversion reaction. Additionally, phase-field simulations describing the process were found to match the experimental results very closely. The nature of the reaction at high rates represents the reaction scenario in a real battery and explains why prior observations have not seen the intercalation reaction profile during lithiation. The work herein provides microscopic insights into reaction dynamics during non-equilibrium conditions and clarifies how the lithium diffusion rate affects the reaction nature in a real battery.

EXPERIMENTAL SECTION

Materials. We have used commercial high-purity Co_3O_4 (>99.5%) nanopowders purchased from US Research Nanomaterials, Inc. The average particle size is about 50 nm. All solvents used, such as ethyl alcohol, were analytically pure and purchased from Fisher Scientific without further purification.

Electrochemical Measurements. The composite electrode used for electrochemical measurements was prepared with 80 wt % active material, 10 wt % carbon black, and 10 wt % polyvinylidene fluoride in *N*-methyl-2-pyrrolidone and cast onto a copper foil current collector. R2032 coin-type cells were assembled inside an argon-filled glovebox with the as-prepared composite electrode as cathode and Li metal as anode. A Celgard 2400 monolayer polyethylene separator and 1 M lithium hexafluorophosphate solution in ethylene carbonate/dimethyl carbonate (DMC) (1:1 in weight) electrolyte were used to make coin cells. Battery testing was performed on an Arbin BT2000 battery test station cycled between 0 and 3 V vs Li^+/Li at room temperature with different current rates (1C, C/10, C/50, C/100). Each current pulse performed on GITT measurement was followed by a 20 h relaxation period to allow full relaxation of the OCV.

TEM Characterization. The samples for *ex situ* TEM were directly removed from the coin cell to a DMC solution inside an argon-filled glovebox after being discharged/charged and then sonicated for 2 min. This solution was subsequently dispersed onto a 300 mesh Cu grid coated with lacey carbon. The *in situ* electrochemical dry cell was assembled onto a Nanofactory TEM/STEM holder inside an argon-filled glovebox and transferred to a TEM column with a sealed argon-filled bag in order to avoid air exposure. Our results (EELS and electron diffraction) show the oxidation with air can be neglected. The *in situ* electrochemical dry cell consisted of a metallic Li coating on a piezo-driven tungsten tip as the negative electrode, Co_3O_4 powder dispersed on half lacey carbon TEM grid as the positive electrode, and Li_2O formed on the surface of Li source as the solid electrolyte. During the lithiation process, a constant negative dc potential was applied between the Co_3O_4 electrode and the Li source (we used 2 and 4 V for the low and high rate discharging, respectively), while capturing the lithiation process in real time by TEM or STEM imaging. *In situ* and *ex situ* TEM characterizations were done on JEOL 2100F TEM equipped with a field-emission electron gun operated at 200 kV and a high-resolution pole-piece with a 0.19 nm point-to-point resolution. For *in situ* LAADF-STEM imaging, the convergence angle is about 12 mrad and the inner collection angle is about 15 mrad. We note that a broad range of collection angles (practically, lower than 50 mrad) can be used for strain-sensitive imaging. Analytical EELS and high-resolution HAADF imaging were performed on a Hitachi-2700C STEM, which equipped with cold field-emission gun and probe aberration corrector. The diffraction data were processed using a script of “DiffTools” of Digital Micrograph (downloaded at <http://www.dmscripting.com/difftools.html>), and the intensity profiles were obtained by using a power law function to subtract the background.

Theoretical Calculation. The DFT calculations were performed using the Vienna Ab initio Simulation Package (VASP) within the projector-augmented wave approach with the Perdew–Burke–Ernzerhof generalized-gradient approximation. The DFT parameters were consistent with the parameters used in Materials Project (MP). A Hubbard U term of 3.32 eV was adopted for Co^{2+} and Co^{3+} in accordance with the MP and the previous testing.^{40–42} The ground-state crystal structures of LiCo_3O_4 were obtained by enumerating a number of ferromagnetic, antiferromagnetic, and ferrimagnetic ordering. The voltage plateaus were obtained using the DFT energies of all relevant compounds in the Li–Co–O ternary space from the MP.⁴³

The phase-field simulation was performed using the electrochemistry theory based on non-equilibrium thermodynamics developed by Bazant *et al.*^{46,47} The details can be found at the [Supporting Information](#).

ASSOCIATED CONTENT

Supporting Information

The Supporting Information is available free of charge on the ACS Publications website at DOI: 10.1021/acsnano.6b04958.

Additional details on pristine material, S/TEM, and theoretical calculation (PDF)

Movie 1 (MPG)

Movie 2 (MPG)

Movie 3 (MPG)
Movie 4 (MPG)
Movie 5 (MPG)
Movie 6 (MPG)

AUTHOR INFORMATION

Corresponding Author

*E-mail: dsu@bnl.gov.

Present Address

¹Department of Materials Science and Engineering and NUANCE Center, Northwestern University, Evanston, IL 60208, USA.

Notes

The authors declare no competing financial interest.

ACKNOWLEDGMENTS

This work is supported by the Center for Functional Nanomaterials, Brookhaven National Laboratory, which is supported by the U.S. Department Of Energy (DOE), Office of Basic Energy Science, under Contract No. DE-SC0012704. Q.M. and Yimei Z. were supported by DOE/BES, Division of Materials Science and Engineering, under Contract No. DE-SC0012704. J.L., H.G., and E.A.S. had additional support for data compilation and analysis as part off the Center for Mesoscale Transport Properties, an Energy Frontier Research Center supported by the U.S. Department of Energy, Office of Science, Basic Energy Sciences, under Award #DE-SC0012673. Yizhou Z. and Y.M. acknowledge the support of the Minta Martin award at University of Maryland, and the computational resources from Extreme Science and Engineering Discovery Environment (XSEDE) supported by National Science Foundation Grant No. TG-DMR130142 and from University of Maryland supercomputing resources.

REFERENCES

- (1) Nitta, N.; Wu, F.; Lee, J. T.; Yushin, G. Li-Ion Battery Materials: Present and Future. *Mater. Today* **2015**, *18*, 252–264.
- (2) Tarascon, J. M.; Armand, M. Issues and Challenges Facing Rechargeable Lithium Batteries. *Nature* **2001**, *414*, 359–367.
- (3) Li, Y.; El Gabaly, F.; Ferguson, T. R.; Smith, R. B.; Bartelt, N. C.; Sugar, J. D.; Fenton, K. R.; Cogswell, D. A.; Kilcoyne, A. L.; Tyliczszak, T.; Bazant, M. Z.; Chueh, W. C. Current-Induced Transition from Particle-by-Particle to Concurrent Intercalation in Phase-Separating Battery Electrodes. *Nat. Mater.* **2014**, *13*, 1149–1156.
- (4) Kang, B.; Ceder, G. Battery Materials for Ultrafast Charging and Discharging. *Nature* **2009**, *458*, 190–193.
- (5) Whittingham, M. S. Ultimate Limits to Intercalation Reactions for Lithium Batteries. *Chem. Rev.* **2014**, *114*, 11414–11443.
- (6) Goodenough, J. B.; Kim, Y. Challenges for Rechargeable Li Batteries. *Chem. Mater.* **2010**, *22*, 587–603.
- (7) Poizat, P.; Laruelle, S.; Grugeon, S.; Dupont, L.; Tarascon, J. M. Nano-sized Transition-Metal Oxides as Negative-Electrode Materials for Lithium-Ion Batteries. *Nature* **2000**, *407*, 496–499.
- (8) Poizat, P.; Laruelle, S.; Grugeon, S.; Dupont, L.; Tarascon, J. M. From the Vanadates to 3d-Metal Oxides Negative Electrodes. *Ionics* **2000**, *6*, 321–330.
- (9) He, K.; Xin, H. L.; Zhao, K.; Yu, X.; Nordlund, D.; Weng, T. C.; Li, J.; Jiang, Y.; Cadigan, C. A.; Richards, R. M.; Doeff, M. M.; Yang, X. Q.; Stach, E. A.; Li, J.; Su, D. Transitions from Near-Surface to Interior Redox upon Lithiation in Conversion Electrode Materials. *Nano Lett.* **2015**, *15*, 1437–1444.
- (10) Thackeray, M. M.; Baker, S. D.; Adendorff, K. T.; Goodenough, J. B. Lithium Insertion into Co₃O₄: A Preliminary Investigation. *Solid State Ionics* **1985**, *17*, 175–181.
- (11) Tao, L.; Zai, J.; Wang, K.; Zhang, H.; Xu, M.; Shen, J.; Su, Y.; Qian, X. Co₃O₄ Nanorods/Graphene Nanosheets Nanocomposites for Lithium Ion Batteries with Improved Reversible Capacity and Cycle Stability. *J. Power Sources* **2012**, *202*, 230–235.
- (12) Fu, Z.; Wang, Y.; Zhang, Y.; Qin, Q. Electrochemical Reaction of Nanocrystalline Co₃O₄ Thin Film with Lithium. *Solid State Ionics* **2004**, *170*, 105–109.
- (13) Larcher, D.; Sudant, G.; Leriche, J. B.; Chabre, Y.; Tarascon, J. M. The Electrochemical Reduction of Co₃O₄ in a Lithium Cell. *J. Electrochem. Soc.* **2002**, *149*, A234.
- (14) Newman, J.; Thomas-Alyea, K. E. *Electrochemical Systems*, 3rd ed.; John Wiley & Sons, Inc., 2004.
- (15) Li, Y.; Tan, B.; Wu, Y. Mesoporous Co₃O₄ Nanowire Arrays for Lithium Ion Batteries with High Capacity and Rate Capability. *Nano Lett.* **2008**, *8*, 265–270.
- (16) Wang, L.; Liu, B.; Ran, S.; Huang, H.; Wang, X.; Liang, B.; Chen, D.; Shen, G. Nanorod-Assembled Co₃O₄ Hexapods with Enhanced Electrochemical Performance for Lithium-ion Batteries. *J. Mater. Chem.* **2012**, *22*, 23541.
- (17) Pan, A.; Wang, Y.; Xu, W.; Nie, Z.; Liang, S.; Nie, Z.; Wang, C.; Cao, G.; Zhang, J. G. High-Performance Anode Based on Porous Co₃O₄ Nanodiscs. *J. Power Sources* **2014**, *255*, 125–129.
- (18) Xu, M.; Wang, F.; Zhao, M.; Yang, S.; Song, X. Molten Hydroxides Synthesis of Hierarchical Cobalt Oxide Nanostructure and Its Application as Anode Material for Lithium Ion Batteries. *Electrochim. Acta* **2011**, *56*, 4876–4881.
- (19) Huang, G.; Xu, S.; Lu, S.; Li, L.; Sun, H. Micro-/Nanostructured Co₃O₄ Anode with Enhanced Rate Capability for Lithium-Ion Batteries. *ACS Appl. Mater. Interfaces* **2014**, *6*, 7236–7243.
- (20) Shaju, K. M.; Jiao, F.; Debart, A.; Bruce, P. G. Mesoporous and Nanowire Co₃O₄ as Negative Electrodes for Rechargeable Lithium Batteries. *Phys. Chem. Chem. Phys.* **2007**, *9*, 1837–1842.
- (21) Wu, Z. S.; Ren, W.; Wen, L.; Gao, L.; Zhao, J.; Chen, Z.; Zhou, G.; Li, F.; Cheng, H. M. Graphene Anchored with Co₃O₄ Nanoparticles as Anode of Lithium Ion Batteries with Enhanced Reversible Capacity and Cyclic Performance. *ACS Nano* **2010**, *4*, 3187–3194.
- (22) Yan, N.; Hu, L.; Li, Y.; Wang, Y.; Zhong, H.; Hu, X.; Kong, X.; Chen, Q. Co₃O₄ Nanocages for High-Performance Anode Material in Lithium-Ion Batteries. *J. Phys. Chem. C* **2012**, *116*, 7227–7235.
- (23) Liu, X. H.; Huang, J. Y. *In Situ* TEM Electrochemistry of Anode Materials in Lithium Ion Batteries. *Energy Environ. Sci.* **2011**, *4*, 3844–3860.
- (24) Liu, H.; Strobridge, F. C.; Borkiewicz, O. J.; Wiaderek, K. M.; Chapman, K. W.; Chupas, P. J.; Grey, C. P. Batteries. Capturing Metastable Structures during High-Rate Cycling of LiFePO₄ Nanoparticle Electrodes. *Science* **2014**, *344*, 1252817.
- (25) Kao, Y. H.; Tang, M.; Meethong, N.; Bai, J.; Carter, W. C.; Chiang, Y. M. Overpotential-Dependent Phase Transformation Pathways in Lithium Iron Phosphate Battery Electrodes. *Chem. Mater.* **2010**, *22*, 5845–5855.
- (26) Chueh, W. C.; El Gabaly, F.; Sugar, J. D.; Bartelt, N. C.; McDaniel, A. H.; Fenton, K. R.; Zavadil, K. R.; Tyliczszak, T.; Lai, W.; McCarty, K. F. Intercalation Pathway in Many-Particle LiFePO₄ Electrode Revealed by Nanoscale State-of-Charge Mapping. *Nano Lett.* **2013**, *13*, 866–872.
- (27) Huang, J. Y.; Zhong, L.; Wang, C. M.; Sullivan, J. P.; Xu, W.; Zhang, L. Q.; Mao, S. X.; Hudak, N. S.; Liu, X. H.; Subramanian, A.; Fan, H.; Qi, L.; Kushima, A.; Li, J. *In Situ* Observation of the Electrochemical Lithiation of a Single SnO₂ Nanowire Electrode. *Science* **2010**, *330*, 1515–1520.
- (28) Gu, M.; Li, Y.; Li, X.; Hu, S.; Zhang, X.; Xu, W.; Thevuthasan, S.; Baer, D. R.; Zhang, J.-G.; Liu, J.; Wang, C. *In Situ* TEM Study of Lithiation Behavior of Silicon Nanoparticles Attached to and Embedded in a Carbon Matrix. *ACS Nano* **2012**, *6*, 8439–8447.
- (29) Wang, C. M.; Xu, W.; Liu, J.; Zhang, J. G.; Saraf, L. V.; Arey, B. W.; Choi, D.; Yang, Z. G.; Xiao, J.; Thevuthasan, S.; Baer, D. R. *In Situ* Transmission Electron Microscopy Observation of Microstructure and

Phase Evolution in a SnO₂ Nanowire during Lithium Intercalation. *Nano Lett.* **2011**, *11*, 1874–1880.

(30) McDowell, M. T.; Ryu, I.; Lee, S. W.; Wang, C.; Nix, W. D.; Cui, Y. Studying the Kinetics of Crystalline Silicon Nanoparticle Lithiation with *In Situ* Transmission Electron Microscopy. *Adv. Mater.* **2012**, *24*, 6034–6041.

(31) McDowell, M. T.; Lu, Z.; Koski, K. J.; Yu, J. H.; Zheng, G.; Cui, Y. *In Situ* Observation of Divergent Phase Transformations in Individual Sulfide Nanocrystals. *Nano Lett.* **2015**, *15*, 1264–1271.

(32) He, K.; Zhou, Y.; Gao, P.; Wang, L.; Pereira, N.; Amatucci, G. G.; Nam, K.-W.; Yang, X. Q.; Zhu, Y. M.; Wang, F.; Su, D. Sodiation via Heterogeneous Disproportionation in FeF₂ Electrodes for Sodium-Ion Batteries. *ACS Nano* **2014**, *8*, 7251–7259.

(33) He, K.; Zhang, S.; Li, J.; Yu, X.; Meng, Q. P.; Zhu, Y.; Hu, E.; Sun, K.; Yun, H.; Yang, X. Q.; Zhu, Y. M.; Gan, H.; Mo, Y. F.; Stach, E. A.; Murray, C. B.; Su, D. Visualizing Non-Equilibrium Lithiation of Spinel Oxide via *In Situ* Transmission Electron Microscopy. *Nat. Commun.* **2016**, *7*, 11441.

(34) Nie, A.; Gan, L. Y.; Cheng, Y.; Asayesh-Ardakani, H.; Li, Q. Q.; Dong, C.; Tao, R. Z.; Mashayek, F.; Wang, H. T.; Schwingschlogl, U.; Klie, R. F.; Yassar, R. S. Atomic-Scale Observation of Lithiation Reaction Front in Nanoscale SnO₂ Materials. *ACS Nano* **2013**, *7*, 6203–6211.

(35) Liu, Y.; Hudak, N. S.; Huber, D. L.; Limmer, S. J.; Sullivan, J. P.; Huang, J. Y. *In Situ* Transmission Electron Microscopy Observation of Pulverization of Aluminum Nanowires and Evolution of the Thin Surface Al₂O₃ Layers during Lithiation-Delithiation Cycles. *Nano Lett.* **2011**, *11*, 4188–4194.

(36) Su, Q.; Du, G.; Zhang, J.; Zhong, Y.; Xu, B.; Yang, Y.; Neupane, S.; Kadel, K.; Li, W. *In Situ* Transmission Electron Microscopy Investigation of the Electrochemical Lithiation Delithiation of Individual Co₉S₈/Co-Filled Carbon Nanotubes. *ACS Nano* **2013**, *7*, 11379–11387.

(37) Luo, L.; Wu, J.; Xu, J.; Dravid, V. P. Atomic Resolution Study of Reversible Conversion Reaction in Metal Oxide Electrodes for Lithium-Ion Battery. *ACS Nano* **2014**, *8*, 11560–11566.

(38) Luo, L.; Wu, J.; Li, Q.; Dravid, V. P.; Poeppelmeier, K. R.; Rao, Q.; Xu, J. Reactions of Graphene Supported Co₃O₄ Nanocubes with Lithium and Magnesium Studied by *In Situ* Transmission Electron Microscopy. *Nanotechnology* **2016**, *27*, 085402.

(39) Muller, D. A.; Nakagawa, N.; Ohtomo, A.; Grazul, J. L.; Hwang, H. Y. Atomic-Scale Imaging of Nanoengineered Oxygen Vacancy Profiles in SrTiO₃. *Nature* **2004**, *430*, 657–661.

(40) He, K.; Lin, F.; Zhu, Y.; Yu, X.; Li, J.; Lin, R.; Nordlund, D.; Weng, T. C.; Richards, R. M.; Yang, X. Q.; Doeff, M. M.; Stach, E. A.; Mo, Y. F.; Xin, H. L.; Su, D. Sodiation Kinetics of Metal Oxide Conversion Electrodes: A Comparative Study with Lithiation. *Nano Lett.* **2015**, *15*, 5755–5763.

(41) Su, Q. M.; Zhang, J.; Wu, Y. S.; Du, G. H. Revealing the Electrochemical Conversion Mechanism of Porous Co₃O₄ Nanoplates in Lithium Ion Battery by *In Situ* Transmission Electron Microscopy. *Nano Energy* **2014**, *9*, 264–272.

(42) Ong, S. P.; Richards, W. D.; Jain, A.; Hautier, G.; Kocher, M.; Cholia, S.; Gunter, D.; Chevrier, V. L.; Persson, K. A.; Ceder, G. Python Materials Genomics (Pymatgen): A Robust, Open-Source Python Library for Materials Analysis. *Comput. Mater. Sci.* **2013**, *68*, 314–319.

(43) Jain, A.; Ong, S. P.; Hautier, G.; Chen, W.; Richards, W. D.; Dacek, S.; Cholia, S.; Gunter, D.; Skinner, D.; Ceder, G.; Persson, K. A. Commentary: The Materials Project: A Materials Genome Approach to Accelerating Materials Innovation. *APL Mater.* **2013**, *1*, 011002.

(44) Jain, A.; Hautier, G.; Ong, S. P.; Moore, C. J.; Fischer, C. C.; Persson, K. A.; Ceder, G. Formation Enthalpies by Mixing GGA and GGA+U Calculations. *Phys. Rev. B: Condens. Matter Mater. Phys.* **2011**, *84*, 045115.

(45) Wang, L.; Maxisch, T.; Ceder, G. Oxidation Energies of Transition Metal Oxides within the GGA+U Framework. *Phys. Rev. B: Condens. Matter Mater. Phys.* **2006**, *73*, 195107.

(46) Bazant, M. Z. Theory of Chemical Kinetics and Charge Transfer based on Nonequilibrium Thermodynamics. *Acc. Chem. Res.* **2013**, *46*, 1144–1160.

(47) Bai, P.; Cogswell, D. A.; Bazant, M. Z. Suppression of Phase Separation in LiFePO₄ Nanoparticles during Battery Discharge. *Nano Lett.* **2011**, *11*, 4890–4896.

(48) Cahn, J. W.; Hilliard, J. E. Free Energy of a Nonuniform System. I. Interfacial Free Energy. *J. Chem. Phys.* **1958**, *28*, 258–267.